



# Influence of carbon based supports on selectivity behavior of diols and propanol in Ru catalyzed glycerol hydrogenolysis

Rasika Mane <sup>a,b</sup>, Shivanand Patil <sup>a</sup>, Masayuki Shirai <sup>c</sup>, Sadhana Rayalu <sup>b,\*,</sup>, Chandrashekhar Rode <sup>a,\*</sup>

<sup>a</sup> Chemical Engineering and Process Development Division, CSIR-National Chemical Laboratory, Pune 411-008, India

<sup>b</sup> Environmental Materials Division, CSIR-National Environmental Engineering Research Institute (CSIR-NEERI), Nagpur 440-020, India

<sup>c</sup> Department of Chemistry and Bioengineering, Iwate University 020-8550, Japan

## ARTICLE INFO

### Article history:

Received 6 August 2016

Received in revised form 17 October 2016

Accepted 15 November 2016

Available online 16 November 2016

## ABSTRACT

Activated carbon (AC) and three graphite materials were studied as supports for Ru catalyzed glycerol hydrogenolysis to propanediols and 1-propanol. Structural characteristics of AC and graphite materials were found to greatly affect the reducibility and particle size of supported Ru and hence, the activity and product distribution in glycerol hydrogenolysis. XRD of graphite materials showed distinctly (002) plane having highly organized layered structure and the peak intensity decreased in the order of Ru/KS150 > Ru/HSAG100 > Ru/KS6 due to decrease in the graphite sheet thickness. In Raman, the intense D band in HSAG100 compared to that in KS6 and KS150 samples indicated its highly amorphous nature or mixed carbon hybridization. Glycerol conversion for Ru on AC was higher than that on graphite and among different graphites, it showed a descending activity order of Ru/KS6 > Ru/HSAG100 > Ru/KS150. The product distribution for AC and HSAG100 supported Ru was similar, giving 1-propanol (45%) alongwith 1,2-propanediol (1,2-PDO) (37%) and 1,3-propanediol (1,3-PDO) (9–11%). For graphite supports, availability of Ru although bigger in size (4–5 nm), would be higher on the surface than in case of AC which formed deep hydrogenolysis products like 1-, 2- propanol, ethanol etc.

© 2016 Elsevier B.V. All rights reserved.

## 1. Introduction

Glycerol is considered as one of the top 12 building blocks derived from bio-mass, with ample availability as a byproduct of biodiesel production and also a safest model polyol possessing versatile reactivity [1]. Particularly, its later attribute allows glycerol to undergo several types of transformations viz. fermentation, oxidation, reduction, dehydration, gasification, carboxylation, esterification etc. into an array of value-added industrial chemicals. Efforts to make such transformations feasible, have direct benefit of improving the process economics of the biodiesel industry [2]. Among several transformations of glycerol, its hydrogenolysis involves selective cleavage of C–O and C–C bonds with simultaneous addition of hydrogen and is regarded as one of the important processes for future biorefineries [3,4]. Depending on the nature of catalyst and process conditions, glycerol hydrogenolysis produces various industrially important chemicals such as 1,2-propanediol

(1,2-PDO), 1,3-propanediol (1,3-PDO), acetol, ethylene glycol (EG), 1-(1-Prop) and 2-propanols (2-Prop). These are commonly used as solvents, in antifreeze formulations and additives in many fields such as polymer (polyesters, polyurethanes), cosmetics and pharmaceuticals [5].

Obviously, more emphasis has been laid on development of catalyst which include noble as well as non-noble metals (Ru, Rh, Re, Ir, Pd, Pt, Au, Cu Ni, Co, Mn, Mo) alone or in combination, optionally on various supports (C, Al<sub>2</sub>O<sub>3</sub>, SiO<sub>2</sub>, ZnO, Amberlyst and zeolites) or in the Raney form (Ni and Cu) or as mixed oxides or salts (Mg, Al, Zn, Ni, Co and Cu) [6–11]. Being a multiproduct reaction with each product having industrial applications, the above studies explored product distribution patterns in glycerol hydrogenolysis, which is still an ongoing effort. Among these catalysts, ruthenium is one of the effective and most studied catalysts for glycerol hydrogenolysis which also produces C–C cleavage products alongwith 1,2-PDO [12]. Activity of Ru catalysts was found to be sensitive to the surface structure, particle size, acidity and basicity of the support and/or nature of the co-catalysts, if used. In particular, nature and type of support material has great influence not only on metal (Ru) dispersion and its particle size but also on catalyst reduction temperature and acidity, all of which in turn greatly affect the activity and

\* Corresponding author.

\*\* Corresponding author.

E-mail addresses: [s.rayalu@neeri.res.in](mailto:s.rayalu@neeri.res.in) (S. Rayalu), [cv.rode@ncl.res.in](mailto:cv.rode@ncl.res.in) (C. Rode).

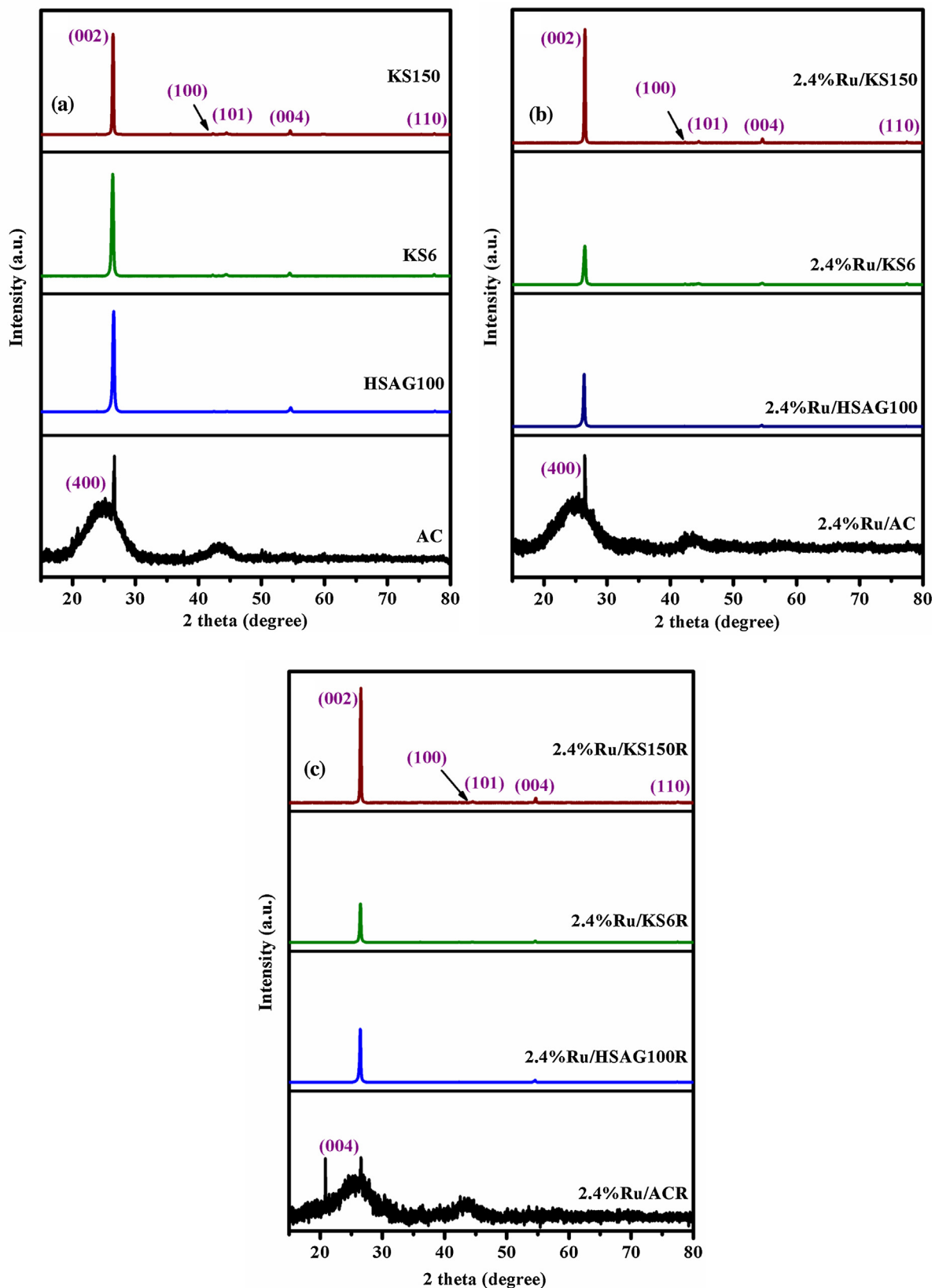


**Fig. 1.** X-ray diffraction patterns of carbon and different grades of graphite. (a) bare, (b) Ru loaded, (c) recovered.

product selectivities. For example, glycerol hydrogenolysis activity per surface Ru atom of Ru/C catalyst was found to increase with increasing Ru particle size (1.2–4.2 nm) while, 1,2-PDO and EG

selectivities changed slightly [13]. In contrast to this, when carbon support was changed to MWNT, Ru particle size increased from 3 to 10 nm resulting in decrease in turnover rate by two-third while, the

selectivity to 1,2-PDO and EG increased significantly (from 32% to 58% and 10% to 21%, respectively) [14]. Interestingly some studies showed that irrespective of particle size and precursor, only higher surface acidity of acid treated activated carbon AC–Ox resulted in higher Ru activity with formation of higher C–O and/or C–C cleavage products (~62%) at the cost of 1,2-PDO (8%) and EG selectivity [15]. Alternately use of additives, sulfurized catalysts, bimetallic compositions or acid co-catalysts, mostly anion exchange resins were attempted for improvement in activity and 1,2-PDO selectivity of Ru catalysts [16–19]. Thus, hydrotalcite supported Ru catalyst modified by Ca, Zn causing the reduction in Ru particle size from 20 to 50 nm to 5–10 nm resulted in higher 1,2-PDO selectivity of >85% [20]. Morphology and size variations were also observed for Ru-bimetallic catalysts on functional supports such as  $\gamma$ -Al<sub>2</sub>O<sub>3</sub>, SiO<sub>2</sub> and ZrO<sub>2</sub> to improve the glycerol hydrogenolysis activity and avoiding the excessive C–C cleavage [21–24]. A systematic study on effect of supports by Feng et al. showed that glycerol hydrogenolysis activity varied in the ascending order as: Ru/SiO<sub>2</sub> < Ru/NaY < Ru/ $\gamma$ -Al<sub>2</sub>O<sub>3</sub> < Ru/C < Ru/TiO<sub>2</sub>, while selectivity towards 1,2-PDO followed the trend, Ru/SiO<sub>2</sub> > Ru/ $\gamma$ -Al<sub>2</sub>O<sub>3</sub> > Ru/C > Ru/NaY > Ru/TiO<sub>2</sub> which was again correlated with the variation in Ru particle size due to support effect [25]. Similarly, in case of basic oxide supports such as CeO<sub>2</sub>, La<sub>2</sub>O<sub>3</sub> and MgO maximum dispersion due to smaller Ru particles of Ru/CeO<sub>2</sub> exhibited maximum activity (85%) [26]. Recently, various forms of carbon such as activated carbon (AC), high surface area graphite (HSAG300), and multi-walled carbon nanotubes (CNT) along with KL-zeolites were found to affect the geometrical and electron characteristics of Ru catalyst which in turn affected the catalytic activity and 1,2-PDO selectivity [27].

From these studies, it was clear that the catalytic activity of Ru for glycerol hydrogenolysis depended on the structural as well as acid-base characteristics, either of the support material or on the type of additives used. In the present work, different carbon sources viz. activated carbon (AC), high surface area graphite (HSAG) and TIMCAL grade graphites (KS6 and KS150, used as support for the first time) were used as supports for Ru catalysts, in order to investigate the effect of structural properties of supports on Ru dispersion, particle size which played a key role in glycerol hydrogenolysis. It was observed that the change in supports from carbon to graphite gave lower glycerol conversion with increased selectivity to deep hydrogenolysis products at the cost of 1, 2-PDO selectivity due to lower surface area and larger Ru particles. While, addition of heteropoly acid (HPA) resulted in formation of 1,3-PDO (10%) and higher selectivity to 1-propanol (46%) along with 1,2-PDO (37%) for all the carbon types used as supports for Ru catalysts.

## 2. Experimental

### 2.1. Catalysts preparation

Activated carbon (AC) was initially treated with sulfuric acid solution (H<sub>2</sub>SO<sub>4</sub> (98%), Merck Limited, India) 10% (v/v) at 333 K for 6 h under constant stirring. Then cooled, filtered and washed with water until pH was neutral (~7) followed by drying in oven at 373 K. Activated carbon supported Ru catalyst was prepared by an impregnation method. In a typical procedure, calculated amount of ruthenium (III) chloride hydrate (RuCl<sub>3</sub>·3H<sub>2</sub>O, Sigma-Aldrich, Bangalore, India) was dissolved in water (~100 mL) to which activated carbon was added and the mixture was refluxed at 353 K for 1 h. After cooling, the mixture was reduced with sodium borohydride (NaBH<sub>4</sub>, Loba Chemie, Mumbai, India) filtered and washed with distilled water until it was Cl<sup>−</sup> free confirmed by silver nitrate LR (AgNO<sub>3</sub>, CHEM LABS, Bangalore, India) test. The resultant solid was dried at 383 K for 12 h.

Graphite supported Ru catalysts were also prepared by the impregnation method in which a calculated amount of graphite support was suspended in 20 mL of distilled water for 15 min. To this slurry, aqueous solution of RuCl<sub>3</sub>·3H<sub>2</sub>O (100 mL) was added drop wise over 30 min. The mixture was stirred under reflux conditions of 373 K for 30 min, after cooling; NaBH<sub>4</sub> was added as a reducing agent. The solid was recovered by filtration and washed with water (~1 dm<sup>3</sup>) until the washings were found to be chloride free. The catalyst was dried (383 K, 12 h) prior to use. Three different grades of graphite were used as a support viz. HSAG100, TIMREX KS6 and TIMREX KS150 and the Ru loaded catalysts were nominated as 2.4% Ru/AC, 2.4% Ru/HSAG100, 2.4% Ru/KS6 and 2.4% Ru/KS150, respectively.

### 2.2. Catalyst characterization

Powder X-ray diffraction patterns were recorded on a P Analytical PXRD system (Model X-Pert PRO-1712), using Ni filtered Cu K $\alpha$  radiation ( $\lambda = 0.154$  nm) as an X-ray source at 30 mA and 40 kV connected with an X-accelerator detector. BET surface area of the adsorbents was determined by N<sub>2</sub> adsorption–desorption technique using Micromeritics-2720 (Chemisoft TPx) volumetric instrument. The metal dispersion was determined by a volumetric adsorption measurement of hydrogen. The apparatus used for the volumetric adsorption measurement of hydrogen was a conventional glass vacuum system. A sample of 0.2 g placed in a Pyrex tube was evacuated at room temperature and initially hydrogen was introduced at room temperature. Then, the sample was reduced at 573 K for 1 h and the amount of hydrogen adsorbed was measured again. The amount of hydrogen adsorbed (H<sub>T</sub>) was measured under  $6.7 \times 10^2$  Pa of equilibrium pressure. After the measurement of total amount of hydrogen adsorbed (H<sub>T</sub>), the sample was evacuated. Again, hydrogen was introduced to the sample at room temperature and the amount of hydrogen adsorbed (H<sub>Rev.</sub>) was measured under  $6.7 \times 10^2$  Pa of equilibrium pressure.

The chemical composition and morphology of the samples were determined by energy dispersive X-ray (EDX) attached to scanning electron microscope (SEM, JEOL JSM 500). A Raman spectrum was recorded using a Horiba JY LabRAM HR 800 micro-Raman spectrometer with 17 mW, 632.8 nm excitation. X-Ray photoelectron spectroscopy (XPS) data of different catalysts were collected on a VG Scientific ESCA-3000 spectrometer using a non-monochromatised Mg K $\alpha$  radiation (1253.6 eV) at a pressure of about  $1 \times 10^{-9}$  Torr (pass energy of 50 eV, electron takeoff angle 55°). The binding energy values were charge-corrected to the C1 s signal (284.6 eV). The transmission electron microscopy (TEM) analysis was performed on a Jeol Model JEM 1200 electron microscope operated at an accelerating voltage of 120 kV. A small amount of specimen was prepared by ultrasonically suspending the powder sample in ethanol, and drop of the suspension was deposited on a carbon coated copper grid dried at room temperature, before analysis. The FT-IR spectra was obtained using a Perkin Elmer frontier instrument in ATR (PIKE make) mode at room temperature. Ammonia temperature programmed desorption (NH<sub>3</sub>-TPD) measurements of all the catalysts were carried out on a Micromeritics-2720 (Chemisoft TPx) instrument. In order to evaluate the acidity of the catalysts, ammonia TPD measurements were carried out by (i) pre-treating the samples from room temperature to 473 K under helium flow rate of 25 mL min<sup>−1</sup> for 2 h, (ii) adsorption of ammonia at 323 K and (iii) desorption of ammonia with a heating rate of 283 K min<sup>−1</sup> starting from the adsorption temperature to 973 K. The total mmol of NH<sub>3</sub> desorbed was calculated by measuring the area of desorption peaks in a low and high temperature regions. The cyclic voltammetry of the catalysts were carried out on Auto-lab PGSTAT30 (Eco-Chemie) instrument having an electrochemical cell with a three electrode system in which glassy carbon was used

as working electrode while Ag/AgCl and graphite rod were used as the reference and counter electrodes, respectively, in 0.1 M HClO<sub>4</sub> as electrolyte. To prepare the working electrode, 5 mg of catalyst was dispersed in 1 mL of (3:1) water: 2-propanol mixture and then adding 40  $\mu$ L of 5% nafion solution, which was sonicated for 1 h. 10  $\mu$ L of the solution was drop coated on the glassy carbon electrode on the area of 0.196 cm<sup>2</sup> dried under IR lamp. The Electrochemical measurement was carried out in an aqueous solution of 0.1 M HClO<sub>4</sub>.

### 2.3. Catalytic reaction

Glycerol hydrogenolysis reactions were carried out in a Parr autoclave of 300 mL capacity. In a typical hydrogenolysis experiment, 10 g of glycerol, 0.8 g of catalyst, 0.5 g of phosphotungstic acid (PTA) as an additive and 90 g of water were charged. The contents were first flushed with nitrogen and then with hydrogen. The reactor was pressurized with H<sub>2</sub> to 5.2 MPa and then heated to the reaction temperature of 493 K. After completion of reaction, the contents were cooled and liquid products were separated by filtration and analyzed by gas chromatography (Shimadzu GC-2025) using a capillary column of FFAP (Free Fatty Acid Phase) (30 m, length  $\times$  0.53 mm, i.d.  $\times$  1  $\mu$ m, film thickness) connected to a flame ionization detector. Gas analysis was carried out using a Shimadzu GC-2014 fitted with ShinCarbon ST, micropacked (100/120 mesh) column (2 m) connected to the TCD detector.

## 3. Results and discussion

### 3.1. Catalysts characterization

In order to understand the differences in the catalytic activity and product selectivities for glycerol hydrogenolysis over Ru supported on AC and three different graphite samples, detail physicochemical characterization of the bare supports, supported Ru as well as spent catalysts was carried out.

XRD patterns of the bare activated carbon showed the amorphous nature as compared to that of graphites (Fig. 1a). The graphite materials showed a sharp, intense peak at  $2\theta = 26.5^\circ$  corresponding to (002) plane of graphite (JSPDS-File 75–1621) having highly organized layered structure with an interlayer spacing of 0.339 nm. The diffraction intensity of this peak (002) decreased in the order of, 2.4% Ru/KS150 > 2.4%Ru/HSAG100 > 2.4%Ru/KS6 due to decrease in thickness of the graphite sheet in the respective samples [28,29]. In other words, sharper the peak at  $2\theta = 26.5^\circ$  (002), thicker the graphite sheet and vice versa meaning that three different grades of graphite were having different number of graphitic layers. The diffraction peak corresponding to the hexagonal (2H) structure was seen at  $2\theta = 42.2^\circ$  (100), while that corresponding to rhombohedral structure (3R) was observed at  $2\theta = 44.4^\circ$  (101), present in all the three different grades of graphite [29]. The additional diffraction peaks at  $2\theta = 53.7^\circ$  (004), 59.8° (103), 77.4° (110) also corresponded to the graphitic structure. XRD patterns of the Ru loaded and spent catalysts (activated carbon and the graphite materials) did not show distinct reflections for the Ru, suggesting the uniform dispersion of the Ru particles on the support (Fig. 1b,c). Supported Ru and recovered catalysts showed the retention of diffraction peaks corresponding to the graphitic structure indicating that no change in the crystallographic properties of the support material occurred after Ru loading and also under reaction conditions.

As seen from Table 1, BET surface area of the activated carbon was much higher ( $600 \text{ m}^2 \text{ g}^{-1}$ ) than that of the graphite material due to its amorphous nature. The surface area of the graphite material decreased in the order of HSAG100 > KS6 > KS150 which was in accordance with the crystallinity of the support material

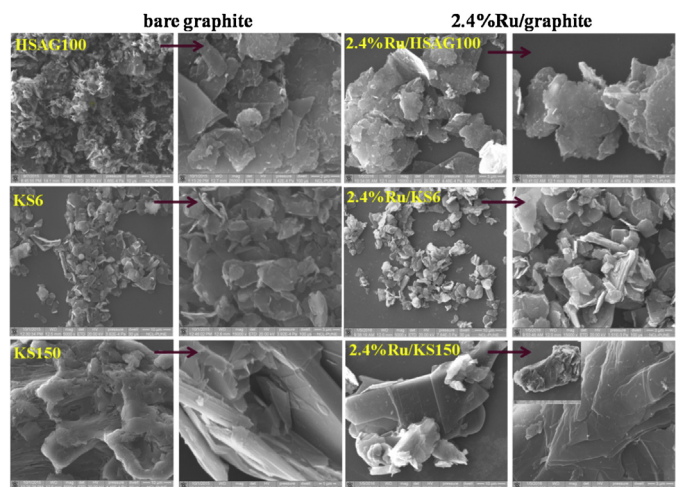


Fig. 2. SEM images of the bare and 2.4%Ru supported different grades of graphite catalysts. The purple colour line shows the higher magnified image of the respective catalyst.

as discussed above. Surface areas of the AC, and HSAG decreased considerably after Ru loading while for KS6 and KS150, surface areas did not change after Ru loading. HSAG100 showed decrease in surface area in the order of, bare ( $126 \text{ m}^2/\text{g}$ ) > 2.4% Ru loaded ( $86 \text{ m}^2/\text{g}$ ) > recovered ( $44 \text{ m}^2/\text{g}$ ). This may be due to some pore blocking of the HSAG100 after Ru loading and aggregation of Ru particles and/or structural changes in graphite material (aggregation of graphite sheets) in the recovered catalyst under high pressure and liquid phase reaction conditions. This was also evidenced from the SEM and TEM analysis which is discussed later. Table 1 also shows that Ru metal dispersion decreased in the order of 2.4%Ru/AC  $\approx$  HSAG100 > KS6 > KS150 which was in accordance with the surface area and the surface functional groups of the respective support material [30]. The absence of functional groups on the catalyst surface leads to a weaker interaction of the metal particles with the support, thus, the probability of crystallite coalescence increases. However, Ru metal dispersion of the HSAG100 and AC was similar, as the HSAG100 shows an intermediate behavior between the ACs and other graphite materials causing high metal dispersion. These results were also supported by the Raman, XPS and TEM analysis as discussed later.

The morphological features of the three different grades of graphite materials and activated carbon and those of Ru loaded and recovered catalysts were observed from SEM analysis (Fig. 2). All the three graphite materials showed a typical feature of flat flake like structure with smooth surfaces having some difference in graphite layered structure. HSAG100 showed small loose graphite sheets of few layers having small dots of carbon like materials. SEM images of KS6 also showed loose thin granules compared to HSAG100 whose size was around few micrometers. SEM image of KS150 clearly showed several folds of graphite sheets that led to its higher crystallinity and decreased surface area as discussed above. Such structural differences of the support materials affecting the dispersion and particle size of the Ru, directly influenced the activity and product selectivities, as discussed later. After Ru loading, no considerable change in the morphology of KS6 and KS150 graphite was observed whereas, HSAG100 showed aggregation of the small graphite sheets around the larger sheet during impregnation of Ru leading to decrease in surface area. Activated carbon showed the typical porous monolith type structure without a change in morphology after Ru loading (Fig. S1). SEM images of the recovered catalysts also didn't show considerable changes in the support materials but with slight aggregation of Ru particles (Fig. S2).

**Table 1**

BET surface area and metal dispersion of the catalysts.

Support	Surface area ( $\text{m}^2/\text{g}$ )			Metal dispersion of fresh 2.4% Ru loaded catalysts (%)
	As it is	2.4%Ru loaded	Recovered	
AC	600	510	552	23
HSAG100	126	86	44	23
KS6	20	20	18	20
KS150	7	8	5.5	7.8

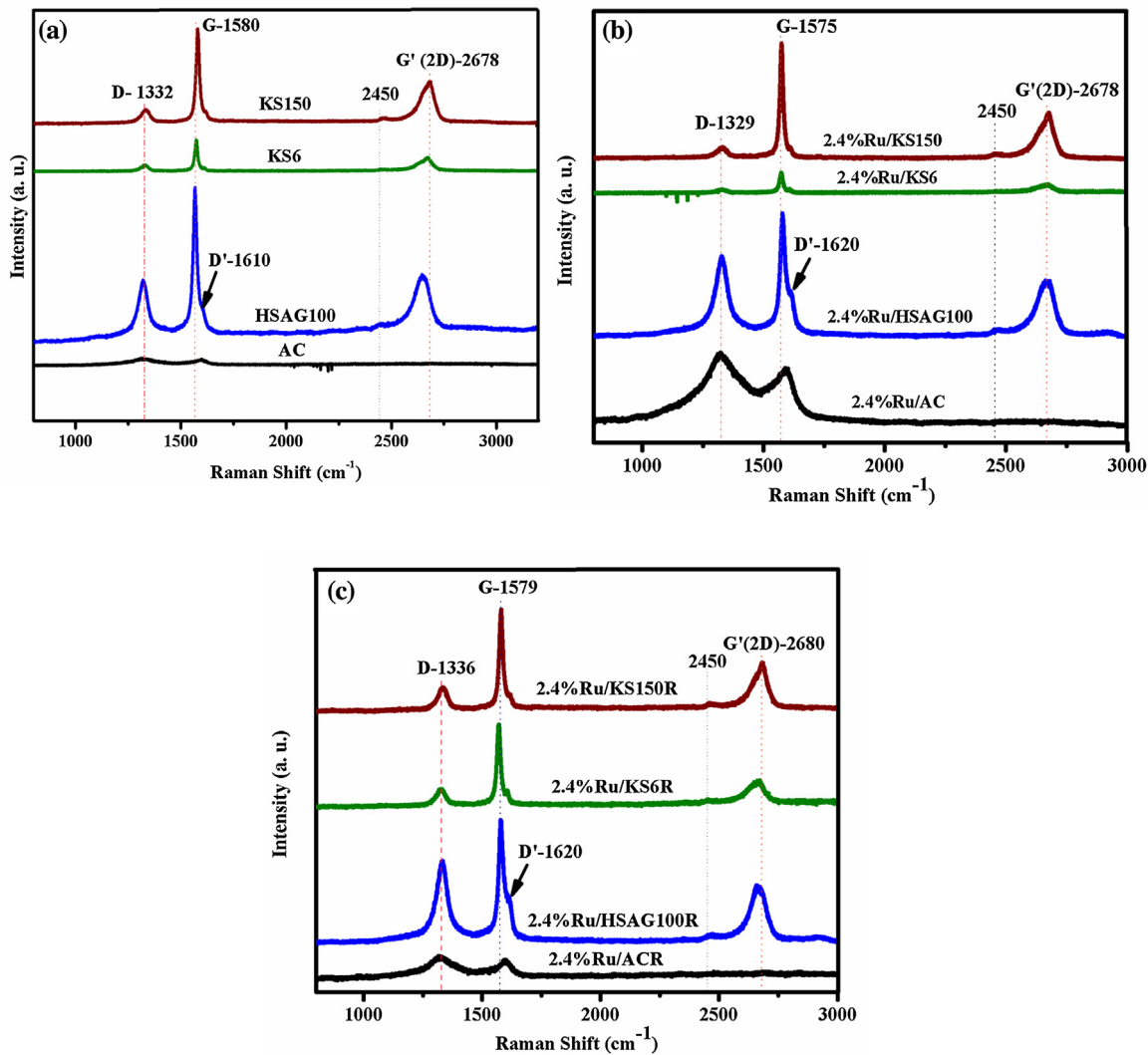


Fig. 3. Raman spectra of (a) bare support, (b) 2.4% Ru supported on AC and graphite materials, and (c) recovered catalysts.

The Raman spectrum was used to determine the defects, ordered and disordered structures of the carbon materials. Fig. 3 compares the 632.81 nm Raman spectra of carbon and three different grades of graphite materials. The carbon and graphite samples showed the characteristic first order D ( $1332\text{ cm}^{-1}$ ) and G ( $\sim 1580\text{ cm}^{-1}$ ) bands of the breathing mode of A1g symmetry involving phonons near the K zone boundary and the E2g mode of graphite involving in-plane bond-stretching motion of  $\text{sp}^2$ -hybridized C atoms, respectively [31]. The appearance of the D band along with intense G band in the graphites indicated that the crystalline graphite structure was having edge defects. The spectrum of all the three carbon allotropes displayed a strong second order G' (2D) signal at  $\sim 2678\text{ cm}^{-1}$  (overtone of the D peak) known to occur in multi-layer graphite structure which was absent in the AC, indicating that

the maximum structural defects were present in AC. In HSAG100 graphite besides the D, G and 2D band, additional D' appeared as a shoulder around  $1620\text{ cm}^{-1}$  on the G band which is the characteristic of the few-layer graphenes with some defects [32]. Such type of D' band was not clearly observed in KS150 and KS6 graphite materials. The intensity of D band in HSAG100 graphite was higher compared to that in KS6 and KS150 samples indicating the higher degree of disorder or the presence of amorphous carbon with mixed hybridization in HSAG100 [33]. The nature and the position of the 2D band in HSAG100, KS6 and KS150 is quite different (Fig. S3). This may be due to difference in the number of graphene layers which decreased in the order of, KS150 > KS6 > HSAG100 [34]. This was in accordance with the BET surface area and XRD results discussed above. There was no significant change in the Raman spectra of the

**Table 2**

Intensity ratio of G to D band and in-plane crystallite size of AC and graphite supports.

Support	$I_G/I_D$			$La$ (nm)		
	Bare	2.4%Ru loaded	Recovered	Bare	2.4%Ru loaded	Recovered
AC	0.9	0.8	0.9	35.3	32	34.7
HSAG 100	2.3	1.5	1.4	88.2	57.2	55.1
KS6	3.4	3	3.4	131.4	115.3	132.1
KS150	5.1	7.1	3.3	195.5	274.7	130

carbon and graphite supported Ru and recovered catalysts indicating that Ru loading and the hydrogenolysis conditions did not affect the structural features of the graphite materials. The intensity ratio of the G- to D-bands (*i.e.*  $I_G/I_D$ ) and the in-plane crystallite size [or size of  $sp^2$  ring clusters (the aromatic domain) in a network of  $sp^3$  and  $sp^2$  bonded carbon] were also calculated using Eq. (1) and are presented in Table 2 [35].

$$La = (2.4 \times 10^{-10}) \lambda^4 \text{laser} (I_D/I_G)^{-1} \quad (1)$$

The  $I_G/I_D$  ratio and the in-plane crystallite size decreased in the order of KS150 > KS6 > HSAG 100 > AC indicating the decrease in the long-range stabilized delocalization of  $\pi$  conjugation structures and/or increased disordered oxidized domain ( $sp^3$  C–C and oxygenated group) [36]. There was no considerable change in the intensity ratio and the  $La$  values of Ru loaded and recovered AC ( $I_G/I_D \sim 0.9$ ,  $La \sim 34.7$  nm) and KS6 graphite ( $I_G/I_D \sim 3.4$ ,  $La \sim 132$  nm) samples. The slight decrease in  $I_G/I_D$  ratio and  $La$  of 2.4%Ru/HSAG100 and recovered KS150 was observed due to some structural changes during the Ru impregnation followed by reduction and the stirring (1000 rpm) during reaction leading to disorder in the layered structure of the KS150, respectively.

X-ray photoelectron spectra of Ru loaded on activated carbon and on graphite supports are shown in Fig. 4. This enabled us to elucidate the surface composition of the AC and graphite materials and the oxidation states of Ru. Fig. 4 shows the combined C1s-Ru 3d core fitting of the 2.4%Ru loaded AC and graphites. In all the samples, C 1s core level framework (surface and bulk) was dominated by a signal at  $\sim 284.3$  eV assigned to the  $sp^2$  and/or  $sp^3$  hybridized carbon framework with slight shifting of BE. The spectral changes observed were due to the influence of the neighboring functional groups or electronic environment. Amorphous carbon consists of the mixture of the  $sp^2$ ,  $sp^3$  and  $sp$  hybridization therefore, the peak at 284.4 eV can be stated as  $sp^2$  and/or  $sp^3$  hybridization [37].

The deconvoluted spectra shows the presence of various oxygen species *viz.* C–OH (285.6 eV), C=O (288.4 eV), C(O)O (290.1 eV) in activated carbon [38] as well as in three different grades of graphite *viz.* HSAG100, KS6 and KS150 (Fig. 4a–d). Along with these peaks, graphite supports gave two additional signals, one at 286.9 eV (C–O–C) and other weak at 291.5 eV ( $\pi$ – $\pi^*$  satellite peak) ascribed to ether/phenolic groups and the delocalized  $\pi$  conjugation (signature of graphitic carbon). The evidence of the C–O functionalities in the graphite support may be due to the lattice defects and grain boundaries created during  $\text{RuCl}_3 \cdot x\text{H}_2\text{O}$  loading under reflux conditions and/or the thermal treatment given to the graphite material. The percentage of these C–O functionalities varied depending on the nature and structural disorder created on the support materials (Table 3). It is known that C–O groups (1,2-ether oxygen) are located on the aromatic carbon atoms, the hydroxyl groups are distributed randomly throughout the carbon basal plane and carboxyl groups are likely to be located at the edges of the graphite sheets [39]. As inferred from Raman analysis, three different grades of graphite materials contained defects which were also justified by the presence of C–O functionalities from XPS analysis.

The oxidation state of Ru was established by a core-level curve fitting on Ru 3d spectra (Fig. 4) however, the corresponding Ru

$3d_{3/2}$  peaks partially interfered with the strong C1s signal from the support. Ru 3d spectra of 2.4%Ru/C revealed the presence of three different species of Ru on the surface *viz.*  $\text{Ru}^0$  evidenced by a doublet at 279.9 and 284 eV separated by 4.1 eV of Ru 3d<sub>5/2</sub> and spin-orbital splitting of Ru 3d<sub>3/2</sub>,  $\text{Ru}^{4+}$  ( $\text{RuO}_2$ ) and  $\text{Ru}^{6+}$  ( $\text{RuO}_3$ ) giving another doublet at 281.3 and 285.4 eV (separated by 4.1 eV) and at 283.3 and 286.9 eV (separated by 3.6 eV), respectively [40]. 2.4% Ru supported on HSAG100 and KS6 graphite showed the predominant presence of the oxidized  $\text{RuO}_2$  and  $\text{RuO}_3$  species with no evidence of metallic Ru. Similarly, 2.4% Ru/KS150 showed a peak corresponding to  $\text{RuO}_2$  species and an additional peak at 282.7 eV ascribed to the kind of Ru oxide but it has been also ascribed controversially to the excitation of Plasmon of Ru-oxide [41]. In any case, it implies that complete reduction of Ru species did not occur with sodium borohydride and/or could originate from the oxidation of Ru during handling and storage in air. The presence of Ru-oxide species could have been also supported by the O 1s spectra of the respective catalysts but these spectra showed overlapping support-related signals. The presence of metallic Ru and its other oxidation states was also confirmed by XPS spectra of Ru 3p<sub>3/2</sub> as shown in Fig. 5(a–d). After deconvolution, the peaks of these samples were observed at binding energies of 460–461.5, 462.4, 463.6 and 465.8 eV corresponding to  $\text{Ru}(0)$ ,  $\text{RuO}_2$ , Ru oxide and plasmon, respectively [42]. Nevertheless, peak intensities of  $\text{Ru}^0$  as well as of oxidized species were different in all the four samples suggesting different extent of reduction.

TEM images were used to investigate the structure and morphology of Ru particles and graphite support. Ru supported on activated carbon showed very small (1.1–1.7 nm) highly dispersed (23%), spherical Ru particles (Fig. 6a). Similarly, Ru/HSAG100 also showed dispersed Ru particles in the range of 1.5–2.5 nm on the edges as well as flat surface of graphene sheet (Fig. 6b1). The formation of smaller Ru particles supported on AC and HSAG100 was due to the higher surface areas and surface oxidized functional groups of the respective supports as discussed above. In contrast to AC and HSAG100 catalysts, the broad range with bigger Ru particles was observed in case of KS6 (1.5–10.5 nm) and KS150 (1–8 nm) supports. Ru supported on KS6 showed an average particle size of  $\sim 5.5$  nm due to the aggregation of Ru particles randomly dispersed on the edges as well as on flat surface of the graphite sheet (Fig. 6c1). However, highly aggregated Ru particles in the range of 2–5.8 nm were observed mainly on edges of the KS150 graphite (Fig. 6d3). This confirmed that the small as well as bigger size Ru particle aggregation was observed on the KS150 support due to its higher crystallinity and lower surface area. The low and high resolution TEM images of the 2.4% Ru/HSAG100 showed transparent, folded, few layered graphene sheets (Fig. 6b,b1). TEM image of 2.4% Ru/KS6 also showed flat graphite sheets with few folds on the surface (Fig. 6c) whereas, TEM of 2.4% Ru/KS150 showed thick and multilayered graphite (Fig. 6d1,d2) sheets with Ru particles on the periphery of the sheet. The folds and/or scrolling is the intrinsic nature of graphene due to its 2D structure that becomes thermodynamically stable *via* bending [43]. The higher magnified image of flat surface of KS150 graphite clearly shows the honeycomb (hexagonal lattice) like structure (Fig. 6d2) without interference of Ru particles. TEM of all the recovered catalysts showed some aggregation giving increased Ru particle size (Fig. S4).

FT-IR of 2.4% Ru supported on AC and three different grades of graphite materials are shown in Fig. 7. The characteristic peaks of oxygen containing functional groups appeared at  $1720\text{ cm}^{-1}$  (C=O stretching vibrations due to COOH and acid anhydride),  $1254\text{ cm}^{-1}$  (C–O and C–OH vibrational mode of epoxide,  $1090\text{ cm}^{-1}$  (C–OH, mainly phenol,) and  $1020\text{ cm}^{-1}$  ( $sp^2$  C–H of cyclic ether or point defect bending modes of –H bonded to aromatic carbon) [44]. The stretching vibrations in the region of 1220 to  $1060\text{ cm}^{-1}$  were mainly due to the unoxidised graphite. Compared to AC, these peaks in graphite materials HSAG100, KS6, and KS150 were very weak,

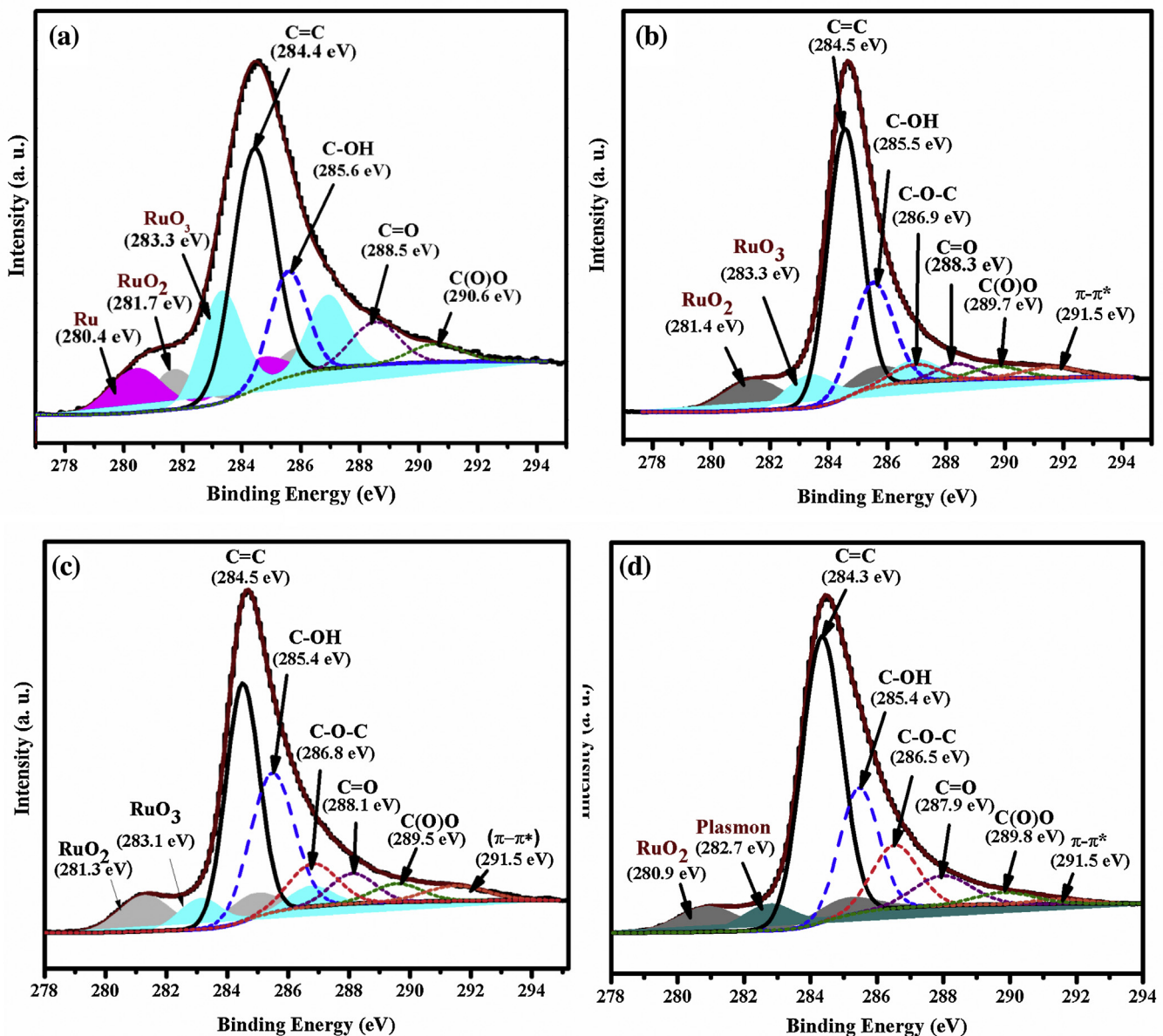


Fig. 4. C1s-Ru3d XPS of (a) 2.4% Ru/AC, (b) 2.4% Ru/HSAG100, (c) 2.4% Ru/KS6, and (d) 2.4% Ru/KS150.

Table 3

The curve fitting data of the C 1s peak with relative area percentage and binding energies (eV).

Sample	C=C/C=C (%)	C—OH (%)	C—O—C (%) ether/phenolic	C=O (%) lac- tone/carbonyl	C(O)O (%) ester/carboxylic
2.4% Ru/AC	284.4 (59)	285.6 (23)	—	288.5 (12)	290.6 (6)
2.4% Ru/HSAG100	284.5 (58.9)	285.5 (27.6)	286.9 (5.2)	288.3 (4.2)	289.7 (4)
2.4% Ru/KS6	284.5 (43.3)	285.4 (33)	286.8 (11.2)	288.1 (7.3)	289.5 (5)
2.4% Ru/KS150	284.3 (52.8)	285.4 (22.6)	286.5 (13.4)	287.9 (7.8)	289.8 (3.2)

as these are synthetic graphite materials and surface functionalities are mainly due to the defect sites. These observations are in accordance with the XPS and Raman spectra as discussed above. Very weak peak at  $1576\text{ cm}^{-1}$  was attributed to  $\text{C}=\text{C}$   $\text{sp}^2$  hybridized in plane vibrations from aromatic zooms. Furthermore, additional peaks at  $2958\text{ cm}^{-1}$  and  $2899\text{ cm}^{-1}$  were due to the stretching vibrations of  $-\text{CH}_3-$  and  $\text{C}-\text{H}$ , respectively [45].

Acid strengths of 2.4% Ru supported catalysts were determined by  $\text{NH}_3$ -TPD studies as shown in Fig. 8. 2.4% Ru on KS6 and KS150 showed two major  $\text{NH}_3$  desorption peaks in the temperature range

of 440–630 K indicating the presence of moderate acid sites. While, 2.4% Ru/HSAG100 was characterized by low intensity peak at 346 K and broad single peak centered at 528 K was due to physically adsorbed  $\text{NH}_3$  (weak acidity) and moderate acid sites, respectively. 2.4 wt% Ru/AC showed two peaks, at  $\sim 354$  K and very broad, valley type peak pattern in the range of 478 to 720 K, indicating the distribution of weak, moderate and strong acid sites [46]. The second peak (at  $\sim 478$  K) could be due to  $\text{NH}_3$  spillover on the support while third peak (at  $\sim 740$  K) could be due to  $\text{NH}_3$  decomposition on the active metal sites at higher temperature [47]. The con-

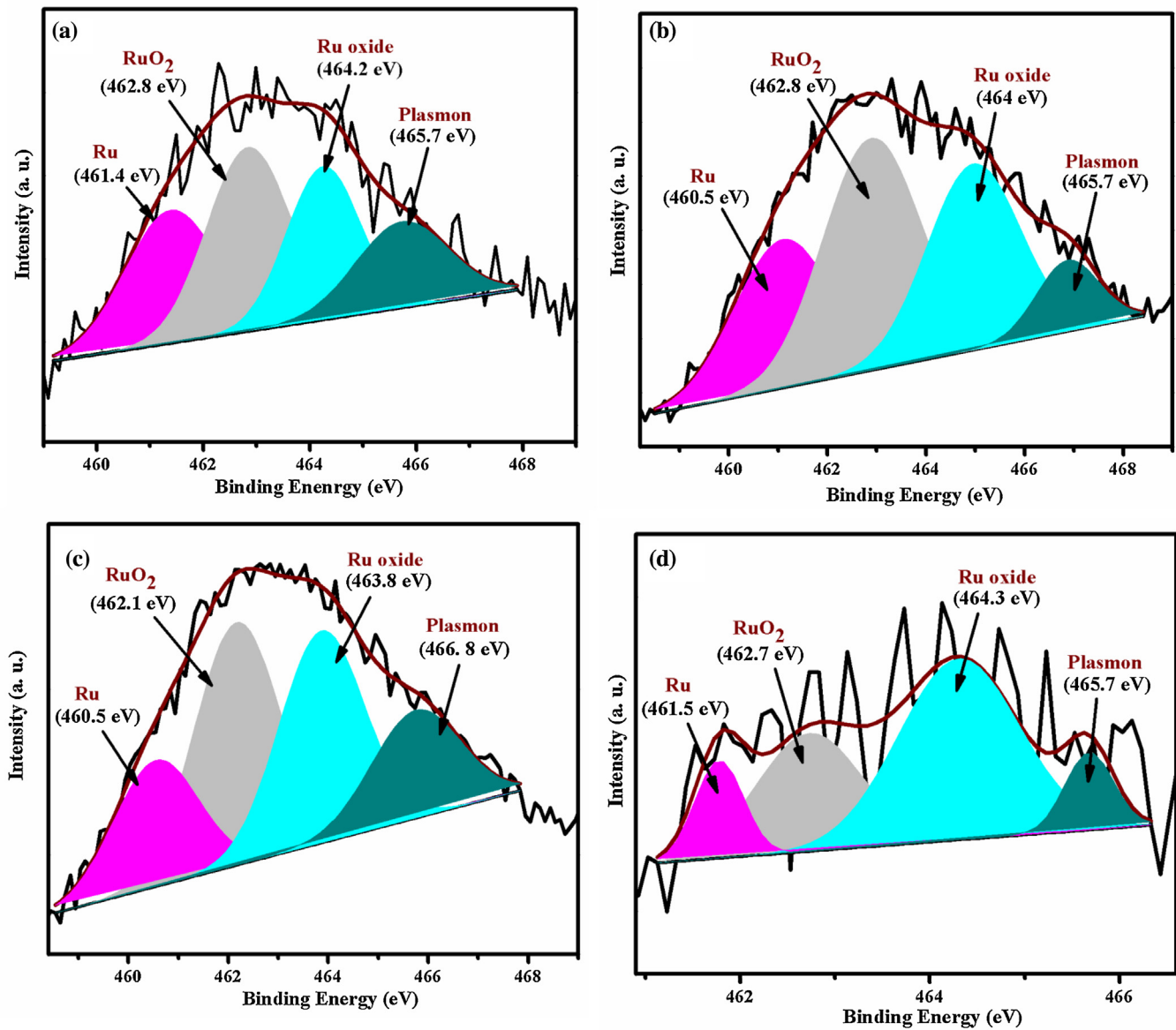


Fig. 5. Ru3p XPS of (a) 2.4% Ru/AC, (b) 2.4% Ru/HSAG100, (c) 2.4% Ru/KS6, and (d) 2.4% Ru/KS150.

centration of the total  $\text{NH}_3$  desorption decreased in the order of 2.4% Ru/AC > 2.4% HSAG100 > 2.4% Ru/KS150 > 2.4% Ru/KS 6 (Fig. 8). The highest acidity of 2.4% Ru/AC was mainly due to presence of acidic functional groups on the surface of activated carbon. Trend of the acidity in case of graphite materials was also in accordance with surface defect sites and/or presence of unreduced surface Ru species. The increase in the weak acidity was mainly due to the generation of new oxidized Ru species, which was not reduced completely during reduction [48]. These results are in accordance with the XPS data and FT-IR spectra as discussed above.

Electrochemical analysis of 2.4% Ru supported catalysts as well as bare activated carbon is shown in Fig. 9. The maximum integrated area for 2.4% Ru/AC catalyst indicated its highest redox potential as compared to the bare AC, 2.4% Ru/HSAG100 and 2.4% Ru/KS150 samples which was ascribed to its (i) large surface area ( $600 \text{ m}^2/\text{g}$ ) or Ru segregation, (ii) smaller particle size (1–1.8 nm) and (iii) reduced amount of Ru oxides [49]. The smaller particle size increased the active surface leading to the higher redox potential. This was also confirmed by the TEM, BET and XRD analysis as discussed previously. The redox potential and/or charge and current associated

with the hydrogen adsorption/desorption regions of the Ru supported on highly crystalline graphite KS150 was low compared with the other supports. This indicated the lower surface area of KS150 supported catalyst. Therefore, the difference in active surface area was responsible for the different catalytic activities of respective catalysts. An anodic peak in the range of 0–0.2 V was attributed to hydrogen desorption from Ru surface [50] while, the broad one in the range of 0.2–0.7 V was ascribed to two stage oxidation of the Ru surface species (Ru (0) to Ru(I) and Ru (II)) due to adsorption of water-related species, such as hydroxyl. The cathodic peak at 0.2 V was attributed to reduction of Ru surface oxide film [51]. In case of 2.4% Ru/HSAG100 and 2.4% Ru/KS150 catalysts, the oxide reduction peak was slightly shifted to higher potential, indicating higher catalyst reducibility. This may be due to the coverage of the electrode by the oxidized Ru species as discussed in XPS analysis.

### 3.2. Glycerol hydrogenolysis

Table 4 shows the screening of AC and graphite supported Ru catalysts with and without PTA as an acid additive for hydrogenol-

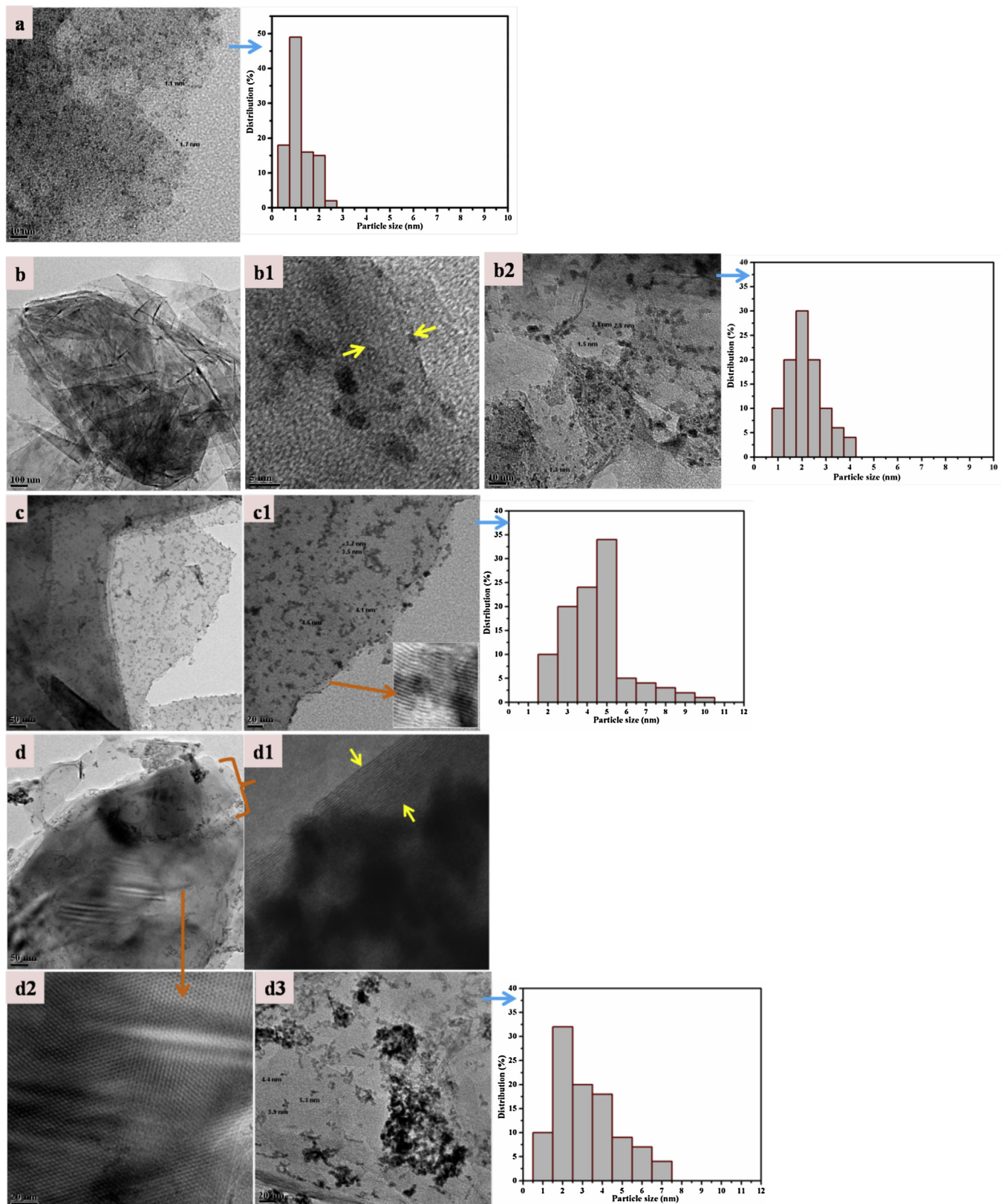


**Fig. 6.** HR-TEM images and the corresponding particle size distribution of (a) 2.4% Ru/AC, (b, b1, b2) 2.4% Ru/HSAG100 with low magnification, higher magnification showing layered structure and higher magnification, respectively, (c, c1) 2.4% Ru/KS6 with low and higher magnification, and (d, d1, d2, d3) 2.4 wt% Ru/KS150 with low magnification, high magnification showing layered structure, honey comb like structure and with Ru particles, respectively.

**Table 4**Activity testing of activated carbon and graphite supported Ru catalysts<sup>a</sup>.

Entry No.	catalyst	con. (%)	TOF (h <sup>-1</sup> )	selectivity (%)										
					1,2-PDO	1,3-PDO	EG	1-Prop	2-Prop	Me-OH	Et-OH	others <sup>d</sup>		
1	2% Ru/AC	44	226	43	10	6	35	1	2	2	0.00	0.3	0.5	0.2
2	2.4% Ru/AC	46	232	37	9	3	45	1	1	2	1	0.2	0.4	0.4
3	2.4% Ru/AC <sup>b</sup>	54	194	31	7	2	55	2	1	0	1	0.3	0.2	0.5
4	2.4% Ru/AC <sup>c</sup>	58	292	55	0	29	1.5	1.5	4	4	1	0.5	1.5	2
5	2.4% Ru/HSAG 100	18	99	37	11	3	44.5	1.5	0.5	1.5	1	–	0.3	0.7
6	2.4% Ru/KS6	23	145	27	6.5	2	53	2	4	1.5	3.5	–	–	0.5
7	2.4% Ru/KS150	13	193	25	7	1.5	44	7	0	0	15	–	0.1	0.4
8	2.4% Ru/HSAG100 <sup>e</sup>	64	281	0	0	0	97	1	0.5	0.5	0	–	0.4	0.6
9	2.4% Ru/KS150 <sup>e</sup>	60	777	0	0	0	97.5	0.5	0.5	0.5	0.5	–	0.2	0.3

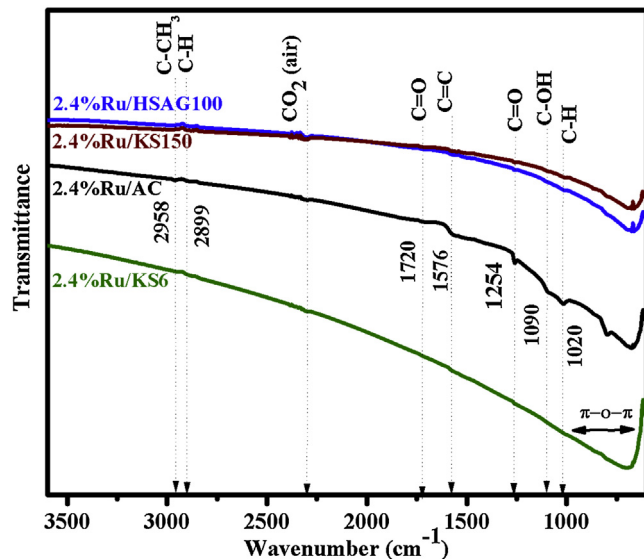
<sup>a</sup> Reaction conditions: 0.8 g catalyst, 0.5 g PTA, 10 wt% aqueous glycerol solution, 493 K temperature, 5.2 MPa H<sub>2</sub> pressure, 5 h.<sup>b</sup> 7 h.<sup>c</sup> Without addition of PTA.<sup>d</sup> Others include acetol, acetone and propanoic acid.<sup>e</sup> 1,2-PDO as a substrate.

Fig. 7. FT-IR spectra of 2.4% Ru supported on AC, HSAG100, KS6, KS150.

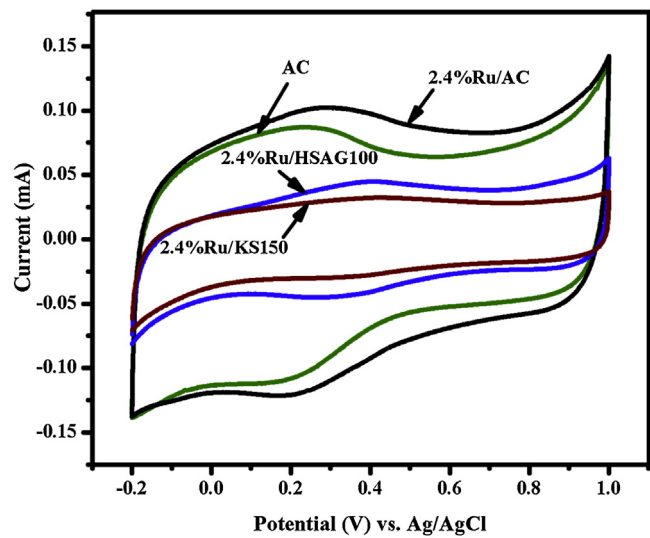
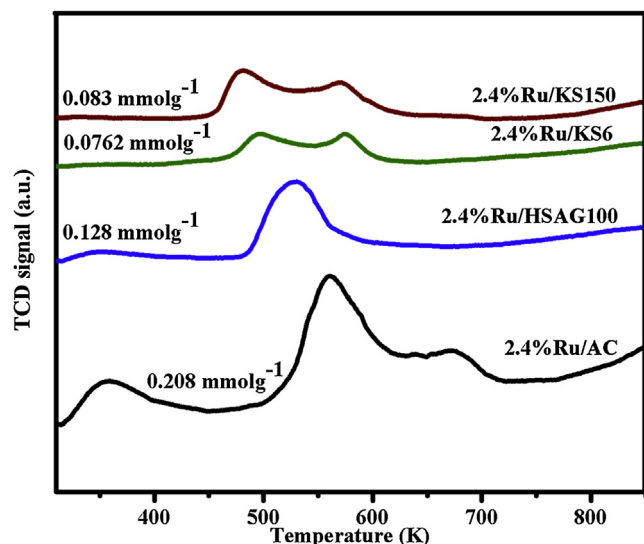


Fig. 9. Cyclic voltammogram of 2.4% Ru supported on AC, HSAG100, KS150 catalysts.

Fig. 8. NH<sub>3</sub>-TPD profiles of 2.4% Ru supported on AC, HSAG100, KS6 and KS150.

ysis of glycerol. Among several other noble metals, Ru was chosen in this work as it poses a better ability to accept  $\pi$  electrons due to higher availability of unoccupied 'd' orbitals. This facilitates the adsorption of carbonyl intermediate such as acetol during glycerol hydrogenolysis [52].

In presence of PTA, 2% Ru/C showed the formation of 1,3-PDO up to 10% along with 1,2-PDO and 1-propanol as major products (Table 4, entry 1). With increase in Ru loading to 2.4%, glycerol conversion increased marginally but interestingly selectivity to 1-propanol increased significantly to 45% with corresponding decrease in 1,2-PDO selectivity (Table 4, entry 2). Similarly, extended reaction time of 7 h enhanced the glycerol conversion from 46% to 54% with corresponding decrease in TOF and selectivity to 1-propanol increased to 55% at the cost of 1,2-PDO selectivity (Table 4, entry 3). Enhancement of 1-propanol selectivity with corresponding decrease in 1,2-PDO selectivity was obviously due to further hydrogenation of diol to 1-propanol, which is also one of the major commodity chemicals [53].

In order to understand the role of PTA in glycerol hydrogenolysis, controlled experiment was carried out without an acid additive (PTA) which gave maximum glycerol conversion of 58% with major selectivities to the C–O and C–C bond cleavage products, 1,2-PDO (53.6%) and EG (37%), respectively, without formation of 1,3-PDO and very less selectivity to excessive hydrogenolysis product, 1-propanol (Table 4, entry 4). This confirmed that the addition of

acid additive (PTA) suppressed the C–C cleavage, facilitating the formation of 1,3-PDO and 1-propanol. 1-propanol formation is possibly by hydrogenation of 1,2-PDO mediated by carbonium ion under acidic conditions [54,55]. Similar observation of formation of 1,3-PDO and 1-propanol was made by ten Dam *et al.* for the glycerol hydrogenolysis over Pd, Pt on  $\text{SiO}_2$  and  $\text{Al}_2\text{O}_3$  catalysts in presence of heteropolyacids [56]. 1,3-PDO formation could be explained through glycerol tungstic acid ester as an intermediate [57,58]. Another important observation was that acetol selectivity was 0.2–3% with acid additives while no acetol formation was observed without an acid additive.

Two reaction routes for glycerol hydrogenolysis to 1,2-PDO and 1,3-PDO, have been proposed involving dehydration and dehydrogenation reactions [1,59]. Under our reaction conditions, glycerol hydrogenolysis proceeded through dehydration route similar to that proposed by Miazawa *et al.* involving metal and acid sites leading to series and parallel reactions (Scheme 1) [60]. Accordingly, first glycerol dehydration gives acetol or 3-hydroxypropionaldehyde on acid sites followed by hydrogenation of intermediates on metal sites to give 1,2- and 1,3-PDO, respectively. In parallel, ethylene glycol was formed through dehydrogenation of glycerol to glyceraldehyde on metal sites followed by retro-alcohol and hydrogenation and/or direct decarbonylation of glyceraldehyde to give EG on the same metal sites. Formation of excessive hydrogenolysis products, 1- and 2-propanol was facilitated due to an acid additive.

As 2.4% Ru/C showed higher selectivity to diols (1,2- and 1,3-PDO) hence, further studies on graphite supports was done with the same Ru loading. Graphitic material was chosen as support as it is another form of carbon but possessing electron donating characteristics that can affect the binding/adsorption of the metal particles to be supported. Three different types of graphitic materials viz. HSAG100, KS6, KS150 were compared with AC as supports for Ru catalyst, in this work. Activity results of Ru on different supports for the glycerol hydrogenolysis are shown in Table 4. In comparison to AC, glycerol conversion decreased for graphite supports in the order of Ru/KS6 > Ru/HSAG100 > Ru/KS150 (Table 4, entries 5–7). However, TOF calculated based on the metal dispersion showed a different trend as Ru/KS150 > Ru/KS6 > Ru/HSAG100. Although Ru metal dispersion on KS150 support was very low (7.8), compared to other supports, the accessibility of active Ru sites was higher (Fig. 6d3) facilitating the glycerol conversion. Interestingly, product distribution obtained for 2.4 wt% Ru/AC and 2.4% Ru/HSAG100 were similar, giving maximum selectivity to 1-propanol (44.5–45%) followed by 1,2-PDO (37%) and 1,3-PDO (9–11%), while the remaining were EG, methanol, ethanol and 2-propanol. Product selectivity pattern obtained for the 2.4 wt% Ru/KS6 was different, showing decreased selectivity to both 1,2- (27%) and 1,3-PDO (6.5%) with a substantial increase in selectivity to degradation products, mainly 1-propanol (53%) along with small amounts of 2-propanol (2%), methanol, ethanol as well as glycerol dehydration product acetol. Ru supported on KS150 exhibited much lower glycerol conversion of 13% with the maximum selectivity to 1-propanol (44%) with again major products as, 1,2-PDO (27%) and 1,3-PDO (6.5%). However, dehydration of both glycerol and 1,2-PDO to acetol (5%) and acetone (7%), respectively proceeded more predominantly (as compared to others) on this catalyst. Another byproduct obtained was the propanoic acid formed due to the acetol isomerization [61,62]. The difference in activity and selectivity results of Ru on various supports were due to the intrinsic properties of supports such as surface area, crystallinity, Ru particle size and its location, *etc.* as discussed below.

Graphite supports having much lower surface area than that of AC, the lowest of  $8\text{ m}^2/\text{g}$  for KS150 (Table 1), also showed the decreasing trend of conversion (Table 4). The difference in activities of Ru/AC and Ru/KS150 was not according to the difference in their surface area but was according to the difference in metal dis-

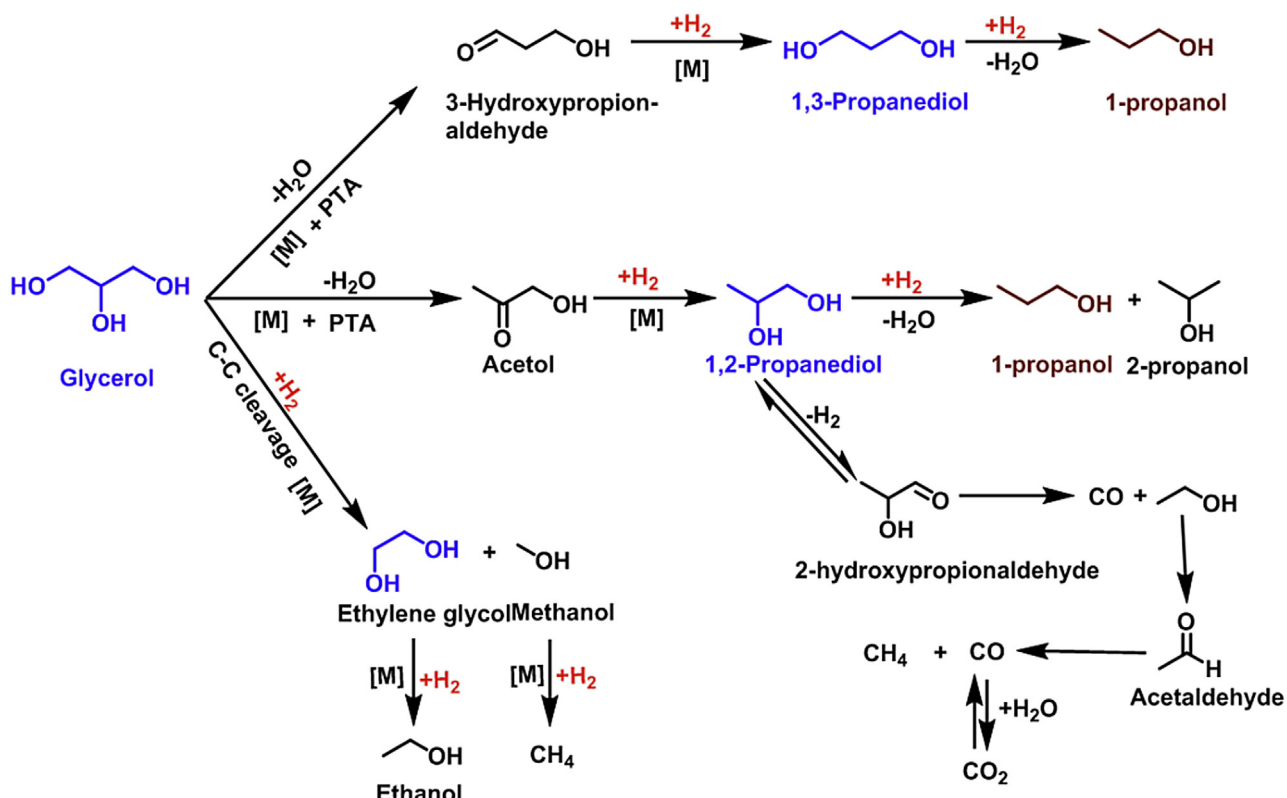
persion. However, Ru/AC catalyst showed the evidence of reduced as well as unreduced Ru species while, in case of Ru/KS150 catalyst, mainly unreduced Ru species were observed (Fig. 4). Since we observed, excessive hydrogenation products such as 1- and 2-propanol, ethanol, *etc.* the formation of reduced Ru species on graphitic supports is expected under reaction conditions. Thus, the direct relation of surface area and/or reduced Ru species with its activity for glycerol hydrogenolysis could not be established, as was also observed in case of Ru on other supports *viz.*  $\text{TiO}_2$ ,  $\text{SiO}_2$ ,  $\text{NaY}$ ,  $\gamma$ - $\text{Al}_2\text{O}_3$  and active carbon [25]. This was also confirmed by conversion and product selectivity *vs.* reaction time profiles shown in Fig. S5 for four different catalysts. All the catalysts showed increase in glycerol conversion and excessive hydrogenolysis product 1-propanol (major) with increase in reaction time. Only 2.4%Ru/KS150 gave slight increase in selectivity to acetol isomerisation and 1,2-PDO dehydration products like propanoic acid and acetone, respectively.

However, nature of the support particularly, crystallinity which was higher for graphites as compared to amorphous nature of carbon (Fig. 1), increased the extent of Ru particle aggregation, dispersion and hence its size as shown by TEM analysis (Fig. 6a–d3) [63,64]. This caused decrease in 1,2-PDO selectivity from 37 to 25% while increasing the selectivity to 1-propanol, 2-propanol, and acetone. This indicated that larger Ru particles (4–5 nm as compared to 1–2 nm for Ru/AC) facilitated the excessive hydrogenolysis. This was in line with the recent studies on zirconia supported Ru catalysts for glycerol hydrogenolysis to 1,2-PDO and EG [52]. In case of graphitic materials due to its layered structure, availability of Ru although higher in size, would be higher on the surface (Fig. 2) than in case of activated carbon having porous structure (Fig. S1). Hence, larger Ru particles on the surface weaken the chemisorption of reactant (glycerol) and products (diols) and favor the availability of surface vacant sites for readsorption of diols leading to deep hydrogenolysis products like 1-, 2- propanol, ethanol *etc.* Control experiments with 1,2-PDO as a substrate over both Ru/HSAG and Ru/KS150 gave higher conversions of 55–65% with selective formation of 1-propanol (Table 4, entries 8,9). The role of larger Ru particles for the formation of excessive hydrogenolysis products was also confirmed by activity testing of the 2.4%Ru/AC400 catalyst having bigger particle size in the range of 2–7 nm (Fig. S6) obtained by calcination followed by activation of catalysts at  $400^\circ\text{C}$  for 3 h. It showed significant increase in selectivity to the excessive hydrogenolysis product, 1-propanol (80%) compared to that of the 2.4 wt% Ru/AC (45%) having smaller Ru particles (0.5–3 nm).

As 2.4% Ru/AC showed the highest glycerol conversion, its stability was confirmed by successful recycle experiments (Fig. S7).

#### 4. Conclusions

Three types of graphite materials such as KS150, HSAG100 and KS6 and activated carbon were investigated as supports for Ru catalyst in the hydrogenolysis of glycerol. SEM image of KS150 clearly showed several folds of graphite sheets that led to its higher crystallinity and lowest surface area. Ru on AC showed very small (1.1–1.7 nm), highly dispersed (23%), spherical Ru particles. Similarly, Ru/HSAG100 also showed Ru dispersion of 23% with particles in the range of 1.5–2.5 nm on the edges as well as on the flat surface of graphene sheet. Ru supported on KS150 showed higher particle size in the range of 2.8 nm to 5.5 nm due to its crystalline nature. XPS studies not only gave the evidence of C–O functionalities in the graphite support arising due to the lattice defects and grain boundaries but also confirmed that Ru species on graphite supports were all in different oxide forms and metallic Ru. This implied metallic Ru responsible for hydrogenation would be formed during hydrogenation reaction itself on the graphite surface. The structural differences of the support materials affecting



**Scheme 1.** Reaction pathways for glycerol hydrogenolysis over noble metal catalysts under acidic condition.

the dispersion and particle size of the Ru directly influenced the activity and product selectivities. Glycerol hydrogenolysis activity was the highest for Ru supported on AC ( $TOF, 232\text{ h}^{-1}$ ) while, glycerol conversion decreased for graphite supports in the order of Ru/KS6 > Ru/HSAG100 > Ru/KS150. Activated carbon and three types of graphite supported Ru nanoparticles gave 1-propanol and 1,2-propanediol as the major products in glycerol hydrogenolysis. However, added phoshotungstic acid led to the formation of 1,3-propadiol and enhanced 1-propanol selectivity, the later by hydrogenation of 1,2-PDO mediated by carbonium ion under acidic conditions. In absence of an acid additive (PTA) glycerol conversion increased from 44 to 58% for AC supported Ru, with major selectivities to the C–O and C–C bond cleavage products without any formation of 1,3-PDO and excessive hydrogenolysis product, 1-propanol was minimum to <2%. This confirmed that the addition of acid additive (PTA) suppressed the C–C cleavage facilitating the formation of 1,3-PDO and 1-propanol.

## Acknowledgements

RBM gratefully acknowledges Council of Scientific and Industrial Research, New Delhi for awarding her CSIR-Nehru Science Postdoctoral Fellowship.

## Appendix A. Supplementary data

Supplementary data associated with this article can be found, in the online version, at <http://dx.doi.org/10.1016/j.apcatb.2016.11.032>.

## References

- [1] A.M. Ruppert, K. Weinberg, R. Palkovits, *Angew. Chem. Int. Ed.* 51 (2012) 2564–2601.
- [2] D.B. Lao, C.E. Alisa, D.M. Heinekey, K.I. Goldberg, *ACS Catal.* 3 (2013) 2391–2396.
- [3] C. Luo, S. Wang, H. Liu, *Angew. Chem. Int. Ed.* 46 (2007) 7636–7639.
- [4] J. Sun, H. Liu, *Green Chem.* 13 (2011) 135–142.
- [5] Y. Nakagawa, K. Tomishige, *Catal. Sci. Technol.* 1 (2011) 179–190.
- [6] V.P. Kumar, S.S. Priya, Y. Harikrishna, A. Kumar, K.V. R, *J. Nanosci. Nanotechnol.* 15 (2015) 1–9.
- [7] Y. Wang, J. Zhou, X. Guo, *RSC Adv.* 5 (2015) 74611–74628.
- [8] R.B. Mane, A.M. Hengne, A.A. Ghalawatkar, S. Vijayanand, P.H. Mohite, H.S. Poddar, C.V. Rode, *Catal. Lett.* 135 (2010) 141–147.
- [9] M.A. Dasari, P. Kiatimkul, W.R. Sutterlin, G.J. Suppes, *Appl. Catal. A: Gen.* 281 (2005) 225–231.
- [10] B. Mallesham, P. Sudarsanam, B.S. Reddy, B.M. Reddy, *Appl. Catal. B: Environ.* 181 (11) (2016) 47–57.
- [11] A.V.-H. Soares, G. Perez, F.B. Passos, *Appl. Catal. B: Environ.* 185 (2016) 77–87.
- [12] C. Wang, B. Dou, H. Chen, Y.C. Song, Y.J. Xu, X. Du, T.T. Luo, C. Tan, *Chem. Eng. J.* 220 (2013) 133–142.
- [13] C. Montassier, J.C. Meíñeiro, L.C. Hoang, C. Renaud, J. Barbier, *J. Mol. Catal.* 70 (1991) 99–110.
- [14] J. Wang, S. Shen, B. Li, H. Lin, Y. Yuan, *Chem. Lett.* 38 (2009) 572–573.
- [15] E. Gallegos-Suarez, M. Pérez-Cadenas, A. Guerrero-Ruiz, I. Rodriguez-Ramos, A. Arcoya, *Appl. Surf. Sci.* 287 (2013) 108–116.
- [16] B. Li, J. Wang, Y. Yuan, H. Ariga, S. Takakusagi, K. Asakura, *ACS Catal.* 1 (2011) 1521–1528.
- [17] D.M. Alonso, S.G. Wettstein, J.A. Dumesic, *Chem. Soc. Rev.* 41 (2012) 8075–8098.
- [18] T. Miyazawa, S. Koso, K. Kunimori, K. Tomishige, *Appl. Catal. A: Gen.* 329 (2007) 30–35.
- [19] P. Centomo, V. Nese, S. Sterchele, M. Zecca, *Top. Catal.* 56 (2013) 822–830.
- [20] S.-H. Leea, D. J. Moon, *Catal. Today* 174 (2011) 10–16.
- [21] E.S. Vasiliadou, E. Heracleous, I.A. Vasalos, A.A. Lemonidou, *Appl. Catal. B: Environ.* 92 (2009) 90–99.
- [22] E.S. Vasiliadou, A.A. Lemonidou, *Org. Process Res. Dev.* 15 (2011) 925–931.
- [23] T. Jiang, Y.X. Zhou, S.G. Liang, H.Z. Liu, B.X. Han, *Green Chem.* 11 (2009) 1000–1006.
- [24] E.P. Maris, W.C. Ketchie, M. Murayama, R.J. Davis, *J. Catal.* 251 (2007) 281–294.
- [25] J. Feng, H. Fu, J. Wang, R. Li, H. Chen, X. Li, *Catal. Commun.* 9 (2008) 1458–1464.
- [26] J. Feng, W. Xiong, B. Xu, W.D. Jiang, J.B. Wang, H. Chen, *Catal. Commun.* 46 (2014) 98–102.
- [27] E. Gallegos-Suarez, A. Guerrero-Ruiz, I. Rodriguez-Ramos, A. Arcoya, *Chem. Eng. J.* 262 (2015) 326–333.
- [28] G. Sun, X. Li, Y. Qu, X. Wang, H. Yan, Y. Zhang, *Mater. Lett.* 62 (2008) 703–706.
- [29] C. Xiu-Yun, *China Int. Nano Lett.* 3 (2013) 1–5.

[30] E. Díaz, S. Ordóñez, R.F. Bueres, E. Asedegbe-Nieto, H. Sastre, *Appl. Catal. B: Environ.* 99 (2010) 181–190.

[31] C.N.R. Rao, K. Biswas, K.S. Subrahmanyama, A. Govindaraj, *J. Mater. Chem.* 19 (2009) 2457–2469.

[32] V. Leoín, M. Quintana, M.A. Herrero, J.L.G. Fierro, A. de la Hoz, M. Prato, E. Vaízquez, *Chem. Commun.* 47 (2011) 10936–10938.

[33] R.B. Heimann, S.E. Esvykov, Y. Koga, *Carbon* 35 (1997) 1654–1658.

[34] L.G. Cancado, K. Takai, T. Enoki, M. Endo, Y.A. Kim, H. Mizusaki, A. Jorio, L.N. Coelho, R. Magalhaes-Paniago, M.A. Pimenta, *Appl. Phys. Lett.* 88 (2006) 163106–1631063.

[35] C. Mattevi, G. Eda, S. Agnoli, S. Miller, K.A. Mkhoyan, O. Celik, D. Mastrogiovanni, G. Granozzi, E. Garfunkel, M. Chhowalla, *Adv. Funct. Mater.* 19 (2009) 2577–2583.

[36] K.S. Kim, Y. Zhao, H. Jang, S.Y. Lee, J.M. Kim, K.S. Kim, J.-H. Ahn, P. Kim, J.-Y. Choi, B.H. Hong, *Nature* 457 (2009) 706–710.

[37] P.K. Chu, L. Li, *Mater. Chem. Phys.* 96 (2006) 253–277.

[38] J.L. Pinilla, H. Puroín, D. Torres, I. Suelves, M. Millan, *Carbon* 81 (2015) 574–586.

[39] D. Yang, A. Velamakanni, G. Bozoklu, S. Park, M. Stoller, R.D. Piner, S. Stankovich, I. Jung, D.A. Field, C.A. Ventrice Jr., R.S. Ruoff, *Carbon* 47 (2009) 145–152.

[40] I.A. Carbalal-Ramos, M.F. Gomez, A.M. Condóa, S. Bengióa, J.J. Andrade-Gamboa, M.C. Abello, F.C. Gennari, *Appl. Catal. B: Environ.* 181 (2016) 58–70.

[41] M.A. Ernst, W.G. Sloof, *Surf. Interface Anal.* 40 (2008) 334–337.

[42] J. Wambach, M. Schuberta, M. Döbelib, F. Vogel, *Chimia* 66 (2012) 706–711.

[43] J.C. Meyer, A. Geim, M. Katsnelson, K. Novoselov, T. Booth, S. Roth, *Nature* 446 (2007) 60–63.

[44] J. Kim, Y. Yamada, R. Fujita, S. Sato, *J. Mater. Sci.* 48 (2013) 8171–8198.

[45] Z. Tang, L. Zhang, C. Zeng, T. Lin, B. Guo, *Soft Matter* 8 (2012) 9214–9220.

[46] W. Raróć-Pilecka, D. Szmigiel, Z. Kowalczyk, S. Jodzis, J. Zielinski, *J. Catal.* 218 (2003) 465–469.

[47] E. Heracleous, A.A. Lemonidou, J.A. Lercher, *Appl. Catal. A: Gen.* 264 (2004) 73–80.

[48] A.A. Bagabas, M. Mokhtar, V.M. Akhmedov, K. Narasimharao, S.N. Basahel, A. Al-Rabiah, *Catal. Lett.* 144 (2014) 1278–1288.

[49] F. Colmati Jr., W.H. Lizcano-Valbuena, G.A. Camara, E.A. Ticianelli, E.R. Gonzalez, *J. Braz. Chem. Soc.* 13 (2002) 474–482.

[50] D. Cao, A. Wieckowski, J. Inukai, N. Alonso-Vantec, *J. Electrochem. Soc.* 153 (2006) A869–A874.

[51] K.S. Nagabushana, E. Dinjus, H. Bönnemann, V. Zaikovskii, C. Hartnig, G. Zehl, I. Dorbandt, S. Fiechter, P. Bogdanoff, *J. Appl. Electrochem.* 37 (2007) 1515–1522.

[52] S. Wang, K. Yin, Y. Zhang, H. Liu, *ACS Catal.* 3 (2013) 2112–2121.

[53] L. Yu, J. Yuan, Q. Zhang, Y.-M. Liu, H.-Y. He, K.-N. Fan, Y. Cao, *ChemSusChem* 7 (2014) 743–747.

[54] M. Schlaf, P. Ghosh, P.J. Fagan, E. Hauptman, R.M. Bullock, *Adv. Synth. Catal.* 351 (2009) 789–800.

[55] Y. Amada, S. Koso, Y. Nakagawa, K. Tomishige, *ChemSusChem* 3 (2010) 728–736.

[56] J. ten Dam, K. Djanashvili, F. Kapteijn, U. Hanefeld, *ChemCatChem* 5 (2013) 497–505.

[57] D.R. Moberg, T.J. Thibodeau, F.G. Amar, B.G. Frederick, *J. Phys. Chem. C* 114 (2010) 13782–13795.

[58] S. Li, D.A. Dixon, *J. Phys. Chem. A* 110 (2006) 6231–6244.

[59] J. ten Dam, U. Hanefeld, *ChemSusChem* 4 (2011) 1017–1034.

[60] T. Miyazawa, Y. Kusunoki, K. Kunimori, K. Tomishige, *J. Catal.* 240 (2006) 213–221.

[61] R.B. Mane, C.V. Rode, *Green Chem.* 14 (2012) 2780–2789.

[62] I. Gandarias, P.L. Arias, J. Requies, M.B. Güemez, J.L.G. Fierro, *Appl. Catal. B: Environ.* 97 (2010) 248–256.

[63] V. Subramanian, J. Choi, E.G. Seebauer, R.I. Masel, *Catal. Lett.* 113 (2007) 13–18.

[64] S. Rojuechai, S. Chavadej, J.W. Schwank, V. Meeyoo, *Catal. Commun.* 8 (2007) 57–64.